Nanoscale Horizons

ROYAL SOCIETY OF CHEMISTRY

COMMUNICATION

View Article Online
View Journal | View Issue

Cite this: *Nanoscale Horiz.*, 2021, 6, 177

Received 2nd December 2020,
Accepted 15th December 2020

DOI: 10.1039/d0nh00672f

rsc.li/nanoscale-horizons

Near-infrared small molecule coupled with rigidness and flexibility for high-performance multimodal imaging-guided photodynamic and photothermal synergistic therapy†

Xiaozhen Li,‡[ab] Fang Fang,‡[c] Bo Sun,[d] Chao Yin,[d] Jihua Tan,[ab] Yingpeng Wan,[ab] Jinfeng Zhang,*[c] Pengfei Sun,[d] Quli Fan,[d] Pengfei Wang,[be] Shengliang Li*[ab] and Chun-Sing Lee*[ab]

Photodynamic therapy (PDT) synergized photothermal therapy (PTT) shows superior clinical application prospects than single PDT or PTT. On the other hand, multimodal imaging can delineate comprehensive information about the lesion site and thus help to improve therapy accuracy. However, integrating all these functions into one single molecule is challenging, let alone balancing and maximizing the efficacy of each function. Herein, a near-infrared (NIR) small molecule (ETTC) with an "acceptor–donor–acceptor" structure was designed and synthesized by coupling rigity and flexibility to simultaneously achieve NIR-II fluorescence imaging (NIR-II FLI), photoacoustic imaging, PTT and PDT. The efficacy of each functionality was well balanced and optimized (NIR-II quantum yield: 3.0%; reactive oxygen species generation: 3.2-fold higher than ICG; photothermal conversion efficiency: 52.8%), which may be attributed to the coupling of the rigid and flexible structures in ETTC to tactically manipulate the energy dissipation paths (non-radiative against radiative decay). As a proof-of-concept, under the effective guidance of local-tumor imaging by PA and whole-body imaging by NIR-II FL, complete tumor eradication was achieved *via* PDT and PTT combinational therapy. This work provides a novel perspective into conceiving and developing single molecule for efficient versatile biomedical applications.

New concepts

Multi-mode imaging-guided therapy has been extensively researched and explored to enhance the imaging quality and improve therapy effect. Currently, multifunctional nanomedicines are mostly obtained by putting multiple components with different functions into one entity. However, this often leads to a compromised reproducibility, difficult operation, and indefinite pharmacokinetics. Thus, achieving a single molecule integrated with multifunction is highly desirable, but challenging. To overcome these challenges, in this work, a small molecule (ETTC) coupled with appropriate rigidity and softness was designed. Taking advantage of the coupled rigid and soft structures, ETTC can tactically regulate nonradiative and radiative decay. Nanoparticles of ETTC demonstrate dual-mode imaging guided photodynamic and photothermal synergistic therapy with well-balanced performance for the four functions *in vitro* and *in vivo*. This work provides a single molecule-based high-performance multifunctional nanotherapeutic for precise medicine, which should motivate researchers to design and explore more novel small molecules coupling optimized toughness with softness for efficient versatile nanomedicines.

Introduction

Complete cancer eradication is especially important for mitigating patients' pain and extending their lifespan.[1–3] Phototherapy, as a promising cancer therapy modality, in which photoenergy is exploited to generate toxic reactive oxygen species (ROS) for photodynamic therapy (PDT) or hyperthermia for photothermal therapy (PTT), has become quite preferred thanks to its attractive advantages, including non-invasiveness, reduced side effects, and good specificity.[4–24] Although great progress has already been made, single-mode PDT or PTT still faces major challenges from intrinsic physiologic barriers, including respective tumor hypoxia or heat resistance,[25–29] which compromises their own therapy effects.

[a] *Center of Super-Diamond and Advanced Films (COSDAF), Department of Chemistry, City University of Hong Kong, 83 Tat Chee Avenue, Kowloon, Hong Kong 999077, P. R. China. E-mail: lishengliang@iccas.ac.cn, apcslee@cityu.edu.hk*
[b] *Joint Laboratory of Nano-organic Functional Materials and Devices (TIPC and CityU), City University of Hong Kong, 83 Tat Chee Avenue, Kowloon Hong Kong SARP. R. China*
[c] *Key Laboratory of Molecular Medicine and Biotherapy, School of Life Sciences, Beijing Institute of Technology, Beijing 100081, P. R. China. E-mail: jfzhang@bit.edu.cn*
[d] *Key Laboratory for Organic Electronics and Information Displays & Jiangsu Key Laboratory for Biosensors, Institute of Advanced Materials (IAM), Jiangsu National Synergetic Innovation Center for Advanced Materials (SICAM), Nanjing University of Posts & Telecommunications, Nanjing 210023, P. R. China*
[e] *Technical Institute of Physics and Chemistry, Chinese Academy of sciences, Beijing 100190, P. R. China*

† Electronic supplementary information (ESI) available. See DOI: 10.1039/d0nh00672f

‡ These authors contributed equally.

This has prompted researchers to explore synergistic therapy combining PDT and PTT.[28,30–34] The PDT/PTT combinational therapy is especially attractive because these not only provide complementary therapeutic modes for covering each other's weakness,[25,30,31] the PTT heating can also accelerate blood flow, which can increase oxygen level at tumors to overcome hypoxia.[25,27] While PDT and PTT have enjoyed much initial success, their wide applications are often limited by the poor tissue penetration depth of visible light. For this reason, extensive efforts have been put into developing PDT and PTT agents that can be activated by near-infrared (NIR) radiation, which have a much longer penetration depth into biological tissues.[28,35–37] However, to date, efficient PDT agents with good performance upon NIR excitation are still rare.

To achieve effective precision phototherapy, high-quality imaging technologies are indispensable. Fluorescence imaging in the second near-infrared window (NIR-II FLI) has demonstrated its advantages over imaging in the visible and NIR-I regions in terms of tissue penetration depth, signal to noise ratio and biocompatibility.[38–50] On the other hand, photoacoustic (PA) imaging provides an alternative technique that utilizes NIR light to trigger ultrasound signals, affording deep penetration and a high temporal–spatial resolution.[20,21,51–57] Impressively, as a tomography technique, PA imaging (PAI) can provide more in-depth information with precise depth measurements.[28,50] Thus, the combined employment of NIR-II and PA imaging can accomplish comprehensive diagnosis with high precision and depth, thus benefiting the subsequent therapy and monitoring. However, as the energy required for achieving PDT, PTT/PAI and NIR-II FLI is competitive, it is difficult to develop a nanotherapeutic to achieve and boost every function efficiency simultaneously.

To address these issues, many efforts have been devoted to designing and developing such multifunctional nanoplatforms. The most employed strategy is to combine many components into one entity to exert their respective functions, and thus to realize multifunctional phototheranostics. Despite its effectiveness, this approach is often associated with poor reproducibility and indefinite pharmacokinetics, severely hindering the progress of clinic translation.[3,28,58–61] Moreover, as the doped components have different optical properties, they often require different excitations from more than one laser, which not only increases the complexity of operation, but also causes treatment delay.[59,60,62] Of note, as 808 nm photosensitizers are rare, thus most versatile nanotherapeutics involving the PDT process can only focus on the NIR region before 808 nm. On the other hand, the reported agents with multimode imaging and therapy performances still have room to be improved for achieving favorable efficiency simultaneously or individually.[58,61,63] Therefore, the development of an 808 nm responsive molecule with intrinsic multifunctionality appears particularly important.

In this work, we developed an "acceptor–donor–acceptor"-structured small molecule (ETTC) with strong NIR absorption. Taking advantages of a coupled hardness with softness structure, the small molecule-based nanotheranostics (ETTC NPs) showed intrinsic multifunctionality, just involving one conjugated oligomer to achieve tetraplex-functional cancer theranostics

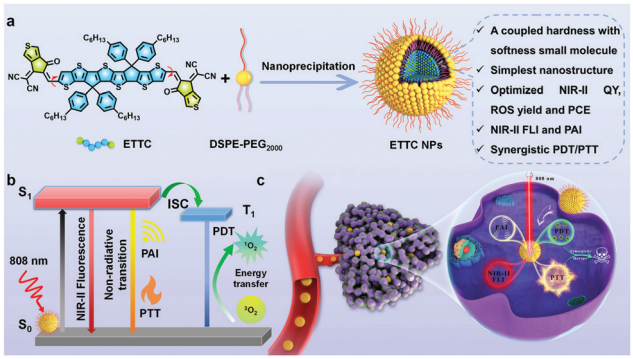

Scheme 1 (a) Preparation of ETTC NPs *via* a nanoprecipitation method. (b) Mechanism of ETTC NPs-based NIR-II FLI, PAI, PTT and PDT. (c) Schematic illustration of ETTC NPs for versatile cancer theranostics.

(NIR-II FLI, PAI, PDT and PTT) (Scheme 1), which successfully addressed the problems induced by the multicomponent construction. Furthermore, the effect of every function was well optimized, realizing an excellent photothermal conversion ability (photothermal conversion efficiency: 52.8%), outstanding singlet oxygen generation performance (3.2-fold higher than ICG) under 808 nm laser illumination, and high NIR-II fluorescence quantum yield (3.0%), surpassing most reported NIR-II fluorophores (Table S1, ESI†). ETTC NPs also possess strong photostability and good biocompatibility. Notably, *in vivo* experiments realized total tumor ablation through a synergistic combination of PTT and PDT under the guidance of dual-mode NIR-II/PA imaging, further confirming the superiority of the ETTC NPs. Therefore, this work provides a new insight for the design and exploration of single molecule-based nanotherapeutics for efficient multifunctional cancer nanomedicines.

Materials and methods

Materials

The raw materials for ETTC synthesis were purchased from SunaTech, Inc. 1,3-Diphenylisobenzofuran (DPBF) and MTT was acquired from Sigma-Aldrich. DSPE-PEG_{2000} was obtained from Avanti Polar Lipids. Hoechst 33342, 2′,7′-dichlorodihydrofluorescein diacetate (DCFH-DA) and all the cell supernatants (DMEM, fetal bovine serum, trypsin buffer, phosphate buffered saline, and antibiotic agents penicillin–streptomycin) were purchased from Thermo Fisher Scientific.

Synthesis of ETTC

The π-conjugated oligomer (ETTC) was synthesized *via* a Knoevenagel condensation.[64,65] Specifically, 6,6,12,12-tetrakis (4-hexylphenyl)-6,12-dihydro-thieno[2″,3″:4′,5′]thieno[3′,2′:4, 5] cyclopenta[1,2-*b*]thieno[2‴,3‴:4″,5″]thieno[2″,3″:3′,4′]cyclopenta [1′,2′:4,5]-2,8-dicarboxaldehyde (CAS No. 2243047-94-9, 57 mg, 0.05 mmol) and 2-(6-oxo-5,6-dihydro-4*H*-cyclopenta[*c*]thiophen-4-ylidene)malononitrile (CAS No. 2099010-83-8, 20 mg, 0.1 mmol) were dropped into a 50 mL two-neck flask and then the dry chloroform ($CHCl_3$, 20 mL) was added as a solvent. Then, pyridine (0.5 mL) was added into the above flask and flushed

with nitrogen. After nitrogen protection, the above mixture was reacted at 65 °C for 24 h. The reaction liquid was cooled to room temperature and then the product was precipitated using 100 mL methanol. Further purification was carried out by column chromatography on silica gel. The product was obtained as a brown solid (32.3 mg, 42%).

Characterization of ETTC

A Bruker Ultra Shield Plus NMR instrument (400 MHz) was used to obtain the ^{1}H NMR spectra of ETTC, respectively. ^{1}H NMR ($CDCl_3$, ppm) δ: 8.76 (s, 2H), 8.33 (d, 2H), 8.06 (s, 2H), 7.91 (d, 2H), 7.20–7.14 (m, 16H), 2.56 (t, 8H), 1.63–1.56 (m, 8H), 1.38–1.21 (m, 24H), 0.85 (t, 12H). ^{13}C NMR ($CDCl_3$, ppm) δ: 181.37, 155.89, 152.73, 149.57, 148.36, 147.59, 143.06, 142.78, 142.49, 142.17, 139.74, 139.07, 138.99, 137.93, 136.78, 129.23, 128.07, 127.79, 127.28, 125.21, 115.23, 114.40, 67.06, 62.49, 35.63, 31.69, 31.23, 29.17, 22.58, 14.08. MALDI-TOF MASS (m/z): 1501.276 ($[M + H]^+$, calculated 1501.370).

Preparation of the ETTC NPs

ETTC itself is not soluble in water, which limits its direct biomedical application as a free molecule. This issue is addressed by packaging the ETTC molecules into water-dispersible nanoparticles. ETTC NPs were prepared *via* a typical nanoprecipitation method. Specifically, 1 mL ETTC solution (1 mg mL^{-1}, dissolved in THF) was homogeneously mixed with 2 mL DSPE-PEG_{2000} solution (5 mg mL^{-1}, dissolved in THF). Then, the mixture was rapidly dropped into 27 mL DI water under vigorous stirring. After leaving overnight, the prepared ETTC NPs were ultrafiltered with 100 kDa millipore and washed three times with PBS. Then, the ETTC NPs were stored at 4 °C in a refrigerator.

Characterization of the ETTC NPs

The loading efficiency is calculated according to the following equation:

$$\text{Loading efficiency} = \frac{\text{Weight of ETTC in nanoparticles}}{\text{Weight of the nanoparticles}} \times 100\%$$

A Malvem Zetasizer Nano ZS instrument and Philips Technai 12 instrument were employed to obtain the DLS and TEM data of the ETTC NPs. A Shimadzu 1700 Spectrophotometer was utilized to get the absorption spectra. A Fluorolog 3 NIR-II system was utilized to acquire the NIR-II emission spectra.

Singlet oxygen generation of the ETTC molecules

ETTC molecules (3 mL, dissolved in THF) containing DPBF were bubbled with oxygen for 8 min, in which the absorption of ETTC at 808 nm and that of DPBF at 415 nm were set to about 0.16 and 1, respectively. The solution was then illuminated using a laser (808 nm, 100 mW cm^{-2}), and its absorption spectra (300–550 nm) were recorded at different post-irradiation times (0, 30, 60, 90, 120, 150, 180, and 210 s). Similar operations were performed on the reference molecules, ICG (3 mL, dissolved in DMSO).

ROS generation of the ETTC NPs

DCFH was used to detect the ROS generated by the ETTC NPs under laser irradiation. In detail, ETTC NPs were diluted with DCFH until the OD value of the NPs reached about 0.2. Then, the ETTC NPs (700 μL) were illuminated using an 808 nm laser (100 mW cm^{-2}), and the fluorescence of DCFH was monitored at different post-irradiation times (0, 1, 2, 3, 4, and 5 min). Similar operations were performed on the reference molecules, ICG water solution.

Photothermal properties tests

ETTC NPs were diluted to different concentrations and then exposed to laser irradiation (808 nm, 1 W cm^{-2}) for 8 min. ETTC NPs (25 μg mL^{-1}) were subjected to different laser powers for 8 min. The temperature profile of the ETTC NPs water dispersions were recorded with a Fluke Ti400 Infrared Camera.

Intracellular ROS detection

DCFH-DA was selected to detect the intracellular reactive oxygen species (ROS) generation ability of the ETTC NPs. Specifically, the same density of A549 cells was cultured in five confocal dishes overnight. Then the culture medium was replaced with five different concentrations of ETTC NPs diluted with DMEM (0, 3.125, 6.25, 12.5, and 25 μg mL^{-1}). After 4 h post-incubation, Hoechst 33342 (16 μM) and DCFH-DA (20 μM) were added to the culture medium at the same time. Then, 30 min later, the cells were washed three times with PBS, and the fresh DMEM was added to the dishes. Then the cells were exposed to an 808 nm laser (1 W cm^{-2}) for 5 min. Finally, CLSM (Leica SPE) was employed to detect the ROS generation ability of the ETTC NPs with different concentrations.

MTT assay

The MTT assay was employed to quantitively assess the biocompatibility and killing ability of the ETTC NPs against A549 cancer cells. For the biocompatibility test, a 96-well plate was seeded with A549 cells (5000/2500 cells per well) and left overnight. Then the cells were incubated with ETTC NPs with different concentrations for 24 h or 48 h, followed by the determination of the cell viabilities by MTT assay. For the killing ability evaluation, a 96-well plate was seeded with A549 cells and left overnight. Then the cells were incubated with different concentrations of ETTC NPs for 4 h when the cells were adherent. Subsequently, the cells were subjected to 808 nm laser irradiation for 5 min. Then 24 h later, the killing ability of the ETTC NPs to A549 cells was determined by MTT assay.

Live/dead staining

Live/dead staining was used to visualize the toxicity of the ETTC NPs to A549 cells. A549 cells with the same density were cultured in four confocal dishes overnight, followed by four different treatment methods: treated with PBS only (control), treated with PBS + laser (808 nm, 1 W cm^{-2}, 5 min, with no NPs), treated with ETTC NPs (25 μg mL^{-1}) only, or treated

with ETTC NPs (25 μg mL^{-1}) + laser (1 W cm^{-2}, 5 min). Then 24 h later, the cells were stained with AM/PI according to the standard protocol. After 30 min, the cells were washed with PBS three times, then the fresh medium was added to the dishes for the subsequent fluorescence imaging by a confocal laser scanning microscope (CLSM, Leica SP5 with IR laser).

Animal model

The nude mice bearing A549 tumor xenograft model was employed for the *in vivo* experiments. To construct the model, 3×10^6 A549 cells (100 μL) were injected into the right flank of the mice *via* the tail vein (BALB/c, female, 5–6 weeks). *In vivo* experiments were conducted when the volume of the A549 tumors grew to about 100 mm^3. The mice for NIR-II imaging were purchased from Jiangsu KeyGEN BioTECH Corp., Ltd, and all related animal experiments were performed according to guidelines approved by the Jiangsu Administration of Experimental Animals. The mice for photoacoustic imaging and cancer therapy were obtained from Beijing Vital River Laboratory Animal Technology Co. Ltd, and all relevant *in vivo* experiments were carried out in accordance with guidelines approved by the ethics committee of Beijing Institute of Technology.

In vivo NIR-II fluorescence imaging

First, 200 μL ETTC NPs (1 mg mL^{-1}) were administrated into the mice *via* the tail vein. Then, NIR-II FLI was performed at specific time points after injection of the ETTC NPs by using a small animal imaging system (Ex: 808 nm laser, filter: 1000–1100 nm).

In vivo photoacoustic imaging

Here, 200 μL ETTC NPs (1 mg mL^{-1}) were intravenously administrated into the mice. After administration, photoacoustic imaging was conducted at specific time points by using a photoacoustic computerized tomography scanner (Endra Nexus 128, Endra Life Sciences, USA).

In vivo photodynamic and photothermal synergistic cancer therapy

The A549 tumor-bearing mice were randomly divided into four groups (6 mice per group) and received four different kinds of treatment: PBS, laser, NPs and NPs + laser. Three mice in every group were sacrificed to dissect tumors after different treatments for hematoxylin and eosin (H&E) staining on the 2nd day after treatment, and the remaining three mice in every group were used to evaluate the therapy effect. An infrared camera (Ti400) was employed to record the tumor temperature. At the 14th day post-treatment, the tumors in every group were excised to weigh.

In vivo ROS evaluation

The A549 tumor-bearing mice were injected with PBS (200 μL) or ETTC NPs (200 μL). Before laser irradiation, the mice were intratumorally injected with 10 μL DCFH-DA solution (10 mM). After laser irradiation, the mice were sacrificed, and the tumor tissues were collected to assess the ROS level by a research slide scanner (VS200, Olympus).

Biosafety evaluation

At the 14th day after treatments, the main organs of the mice in every groups were exercised for H&E staining. Blood samples of the mice were collected for blood biochemical analysis. Six hematological indexes of the mice, including alanine aminotransferase (ALT), blood urea nitrogen (BUN), lactate dehydrogenase (LDH), aspartate transaminase (AST) and alkaline phosphatase (ALP), were analyzed using a Chemray 800 Automated Chemistry Analyzer (Shenzhen Rayto Life and Analytical Sciences).

Results and discussion

Design, synthesis, and characterization of the ETTC and ETTC NPs

To simultaneously obtain good photoacoustic, NIR-II fluorescence, photodynamic, and photothermal properties, the molecule should possess: (1) a narrow energy gap (E_g) to facilitate effective NIR absorption; and (2) a small energy offset (ΔE_{ST}) between singlet and triplet excited states to enable efficient intersystem crossing (ISC).[66–68] To further balance and optimize the efficacy of each function, the molecule should have a coupled flexibility and rigidity structure. A flexible molecular structure on the one hand can promote heat generation,[69] while on the other hand it would also hinder intermolecular aggregation minimizing fluorescence quenching.[70] A rigid structure as a motionless part prevents excessive heat dissipation and enables fluorescence intensity enhancement. Thus, a molecule coupled with an appropriate structure of flexibility and rigidity would endow the system with a balanced heat and fluorescence generation *via* tactically modulating the energy flow directions. With these considerations, we introduced a strong electron acceptor (A) and an effective donor (D) to construct a "A–D–A" structured small molecule (ETTC) (Fig. S1, ESI†). The identity of the ETTC was confirmed with ^{1}H NMR, ^{13}C NMR, and mass spectra (Fig. S2–S4, ESI†). The molecule has a small energy gap of 1.83 eV, enabling absorption over the NIR region. Meanwhile, the ΔE_{ST} was calculated to be 0.65 eV using density functional theory (DFT). Such a small ΔE_{ST} can promote the ISC process, which is beneficial for ROS generation.[66] In ETTC, both the D and A moieties are of high rigidity and they are linked *via* two C–C bonds, which allow the two A moieties to freely rotate with respect to the central D backbone. The dihedral angle between the donor and acceptor plane is only 1° (Fig. S5, ESI†), indicating a very small steric hindrance, which is favorable to the relative rotation.

The optical absorption of ETTC in tetrahydrofuran (THF) was measured with a UV-vis-NIR spectrometer, showing an absorption peak at 750 nm with a high mass extinction coefficient of 130.3 L g^{-1} cm^{-1} (Fig. S6, ESI†), which is much higher than that of the reported agents.[35,37,71–73] ETTC molecules were then assembled into water-dispersible nanoparticles (ETTC NPs) with an amphiphilic polymer DSPE-PEG_{2000} (Scheme 1a). The loading efficiency was determined to be 6.2%.

Dynamic light scattering (DLS) and transmission electron microscopy (TEM) were employed to measure the size and morphology of the ETTC NPs. As shown in Fig. 1a and b, the NPs had a spherical shape and an average hydrodynamic diameter of 59.3 nm. The zeta potential of the ETTC NPs was measured to be −23.1 eV (Fig. S7, ESI†). Compared with the molecules dissolved in THF (Fig. S6, ESI†), the NPs aqueous dispersion showed a broadened and red-shifted absorption (Fig. 1c, left). The ETTC NPs exhibited strong fluorescence from 900 to 1200 nm under 808 nm laser excitation (Fig. 1c, right). According to the reported protocol, the NIR-II quantum yield (NIR-II QY) of ETTC NPs was determined to be 3.0% (Fig. S8, ESI†), which is higher than those of most reported NIR-II FL nanoagents (Table S1, ESI†).[74] These attractive properties make the ETTC NPs promising for biomedical applications.

ROS generation of the ETTC and ETTC NPs

We first investigated the ROS generation ability of the ETTC molecules and ETTC NPs under 808 nm laser irradiation (100 mW cm^{-2}). Singlet oxygen generation by the ETTC molecules dissolved in THF was detected with 1,3-diphenylisobenzofuran (DPBF), where the absorption at 415 nm can be quenched upon reaction with singlet oxygen. ICG was used as a comparison standard. Fig. 1d and e, respectively, show the absorption spectra of DPBF after 808 nm irradiation for different durations with ICG and ETTC. It can be seen that ETTC showed a much faster generation rate of singlet oxygen (~7.5 times of ICG, Fig. 1f), while DPBF alone (control) could not generate singlet oxygen (Fig. S9, ESI†). Dichlorodihydrofluorescein (DCFH) was selected as the probe to evaluate the ROS production ability of the ETTC NPs in water. It can be seen that the fluorescence intensity of DCFH containing ICG solution (Fig. 1g) or ETTC NPs aqueous dispersion (Fig. 1h) increased with duration of irradiation, while that of the DCFH alone (control) showed a negligible increase (Fig. S10, ESI†). These data are summarized in Fig. 1i which shows that the ROS generation rate of ETTC NPs was ~3.2 times that of ICG. These suggest that the ETTC NPs have a remarkable capability for ROS generation and thus good potential for PDT applications.

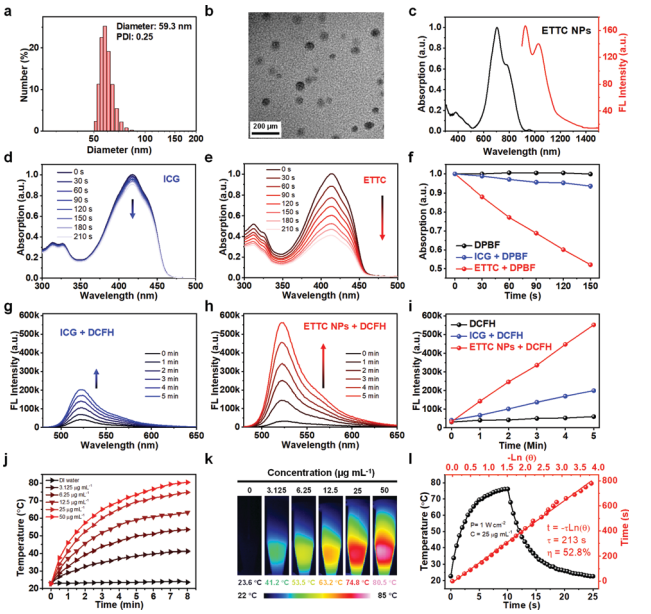

Fig. 1 (a) DLS analysis; and (b) TEM image of the ETTC NPs. (c) Absorption and emission spectra of the ETTC NPs in water. Absorption decrease of DPBF upon irradiation with an 808 nm laser (100 mW cm^{-2}) in the presence of (d) ICG; and (e) ETTC molecules. (f) Absorption decrease of DPBF at 415 nm with increasing irradiation time. Fluorescence intensity increase of DCFH upon irradiation with an 808 nm laser (100 mW cm^{-2}) in the presence of (g) ICG; and (h) ETTC NPs. (i) Fluorescence intensity increase of DCFH at 525 nm with increasing irradiation time. (j) Temperature-elevating curves of aqueous dispersions of ETTC NPs with different concentrations and DI water under 808 nm laser illumination (1 W cm^{-2}). (k) Corresponding photothermal images of the ETTC NPs aqueous dispersions after 5 min of laser irradiation. (l) Temperature-increasing/decreasing curve, and cooling time *vs.* −ln(θ) plot (θ: temperature driving force).

Photothermal properties of the ETTC NPs

The photothermal performance of the ETTC NPs was then studied. Temperature-rising curves of the ETTC NPs aqueous dispersions of different concentrations and DI water were recorded under 808 nm laser irradiation. The ETTC NPs showed efficient photothermal conversion, and the heating effect increased with the rising concentration (Fig. 1j) and laser power (Fig. S11, ESI†). Photothermal imaging further confirmed the excellent thermal-generation capacity of the ETTC NPs (Fig. 1k). The photothermal conversion efficiency (PCE) of the ETTC NPs was determined to be 52.8% (Fig. 1l). We also evaluated the photostability of the ETTC NPs. After laser irradiation, the absorption curve was measured and it showed no observable difference to that before laser irradiation (Fig. S12, ESI†). In addition, no declining trend in the temperature-climbing ability of the ETTC NPs was observed even after five heating/cooling cycles (Fig. S13, ESI†). These results demonstrate the outstanding photothermal conversion efficiency and good photostability of the ETTC NPs for potential PTT applications.

Intracellular ROS generation and cytotoxicity evaluation

Cell experiments were further conducted to validate the ROS generation ability of ETTC NPs. 2′,7′-Dichlorodihydrofluorescein diacetate (DCFH-DA) was used as an intracellular ROS detection probe. Here, DCFH-DA will first be hydrolyzed into DCFH by intracellular esterases after internalizing into cells. Upon oxidization by ROS, DCF with a fluorescent peak at 525 nm would be formed. Fig. 2a show that with no NPs, green fluorescence from DCF could not be detected in A549 cells. As the concentration of the ETTC NPs increased, the green fluorescence from DCF increased. It is interesting that even with a very low ETTC NPs concentration of 3.125 μg mL^{-1}, intracellular ROS generation could be clearly observed, demonstrating the good ROS production performance. Moreover, quantification analysis of the green fluorescence intensity from DCF indicated a concentration-dependent ROS generation in the range from 0 to 25 μg mL^{-1} (Fig. 2b). Endowed with an excellent photothermal conversion and ROS generation ability, cytotoxicity experiments were subsequently performed using A549 cell lines with the standard MTT assay. As exhibited in

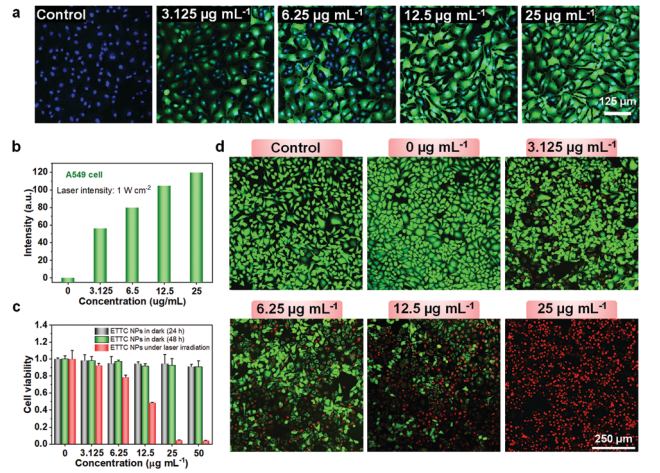

Fig. 2 (a) Visualization of ROS generation from ETTC NPs with different concentrations using DCFH-DA under laser exposure (blue: Hoechst 33342 channel; green: DCFH-DA channel). (b) Quantification of the ROS level in A549 cells. (c) Cytotoxicity of different concentrations ETTC NPs in the dark (incubation for 24 h or 48 h) or under laser irradiation for 5 min (808 nm, 1 W cm^{-2}). (d) Live/dead staining of A549 cells.

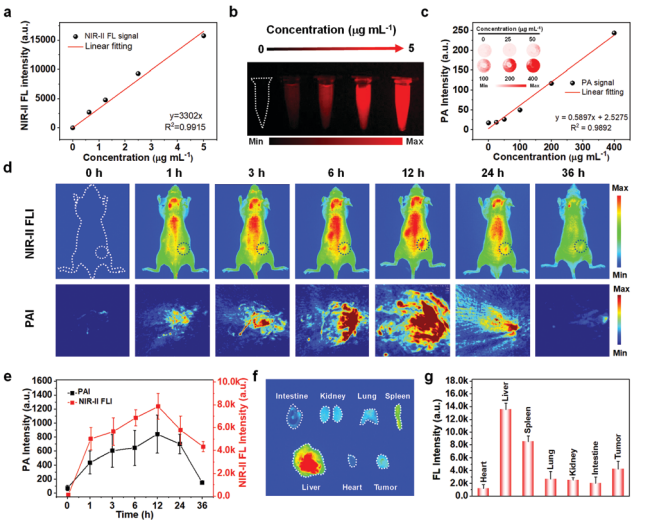

Fig. 3 (a) NIR-II fluorescent intensity (1000–1100 nm) as a function of the ETTC NPs concentration in water. (b) Corresponding fluorescent images of the samples in (a). (c) PA signal intensity as a function of NPs concentration. Inset shows the corresponding PA images. (d) *In vivo* NIR-II images of the mice and PA images of the tumor site after intravenous administration of the ETTC NPs. (e) PA/NIR-II FL intensity at the tumor site after injection of the ETTC NPs. (f) NIR-II images of the main organs and tumor at 12 h post-injection of the ETTC NPs. (g) NIR-II FL intensity of the main organs and tumor.

Fig. 2c, the ETTC NPs in the dark showed little cytotoxicity, but upon laser irradiation, a high cell-fatality rate of over 95% was observed. To vividly depict the cancer cell-killing ability of the ETTC NPs, we utilized AM/PI staining to visualize the cell-death phenomenon. The results showed that the laser itself (without NPs) had a negligible effect on A549 cell viability, while the ETTC NPs showed increasing toxicity to A549 cells with their increasing concentration under laser irradiation for 5 min. Notably, A549 cells were almost completely annihilated with an ETTC NPs concentration of 25 μg mL^{-1} (Fig. 2d). These results revealed that the ETTC NPs have good biocompatibility and cancer cell-eradication capability.

In vivo NIR-II FL and photoacoustic imaging

High-quality and complementary imaging technologies are indispensable for precise and effective cancer therapy, and can function as a "navigator" in the therapy process. Here, we employed two imaging modalities, NIR-II and PA imaging, for tumor diagnosis. Fig. 3a shows that the fluorescent intensities of the 1000–1100 nm emission were directly proportional to the concentration of the ETTC NPs in aqueous dispersion. This proportional relationship is particularly convenient for quantitative image analysis. It is particularly impressive that a zero fluorescent signal was obtained when there were no NPs present. This will ensure high contrast images with no background noise for bioimaging (Fig. 3b). Fig. 3c shows that the PA signal intensity increased linearly with the NPs concentration. The inset shows the corresponding PA images. Subsequently, an A549 tumor xenograft nude mice model was employed for *in vivo* imaging. As expected, NIR-II FL and PA imaging showed similar signal-evolution trends at the tumor site after intravenous injection of the ETTC NPs. The signal intensity gradually increased in the first 12 h followed by a signal decrease in the following time points (Fig. 3d and e). Thus, 12 h post-injection of the ETTC NPs was selected as the optimal treatment time point. Moreover, the main organs and tumor of the mice were dissected to examine the distribution of ETTC NPs *via* NIR-II FL imaging. The results showed that most of the nanoparticles entered into the liver, spleen, and tumor (Fig. 3f and g). Such an effective accumulation of nanoparticles at the tumor location is advantageous for cancer therapy.

In vivo anti-tumor performance

In vivo cancer elimination experiments were carried out to examine the therapeutic effect of the ETTC NPs. Mice bearing the xenograft A549 tumor were randomly divided into four groups (6 mice per group) and received four different kinds of treatment when the tumor size reached ~100 mm^3. The first group of mice were injected with only PBS (PBS), the second group was injected with PBS and irradiated with 808 nm laser for 10 min at 12 h post-injection (laser), the third group was injected with only ETTC NPs (NPs), and the fourth group was injected with ETTC NPs and irradiated with 808 nm (NPs + laser). In particular, three mice in every group were monitored for 14 days, while the remaining three mice in every group were sacrificed for tumor hematoxylin and eosin (H&E) staining on the 2nd day after treatment. An infrared camera was employed to record the tumor temperature of the mice treated with the laser or NPs + laser. Compared with the mice treated with the laser, the tumor temperature of the mice treated with the NPs + laser grew much more quickly (Fig. 4a and b), verifying the good photothermal conversion ability of the ETTC NPs. After treatment, only the tumors in the mice treated with NPs + laser disappeared, while the tumors in the mice that received the

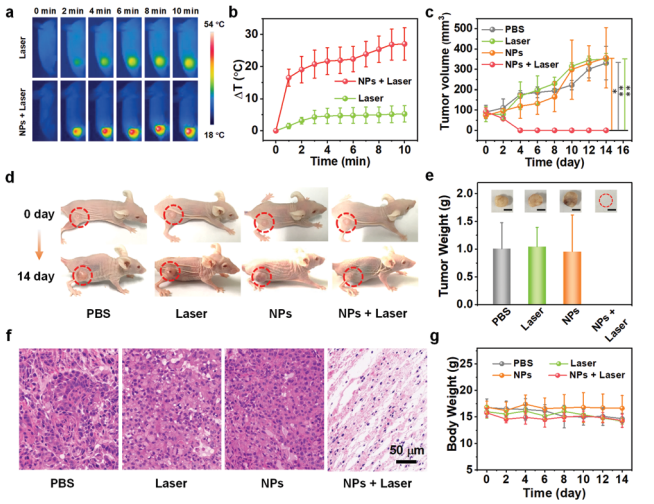

Fig. 4 (a) Photothermal imaging of A549 tumor-bearing nude mice under laser irradiation (808 nm, 1 W cm^{-2}) for 10 min. (b) Temperature variations at the tumor site with the increasing irradiation time. (c) Tumor volume evolution after the different treatments (*$p < 0.05$; **$p < 0.01$; one-way analysis of variance (ANOVA)). (d) Representative graphs of the mice taken from day 0 and day 14 for the different treatments. (e) Tumor weights in the different groups (scale bar: 0.5 cm). (f) H&E staining of tumors isolated from the mice with different treatments. (g) Body weight change of the mice in the different groups within 14 days.

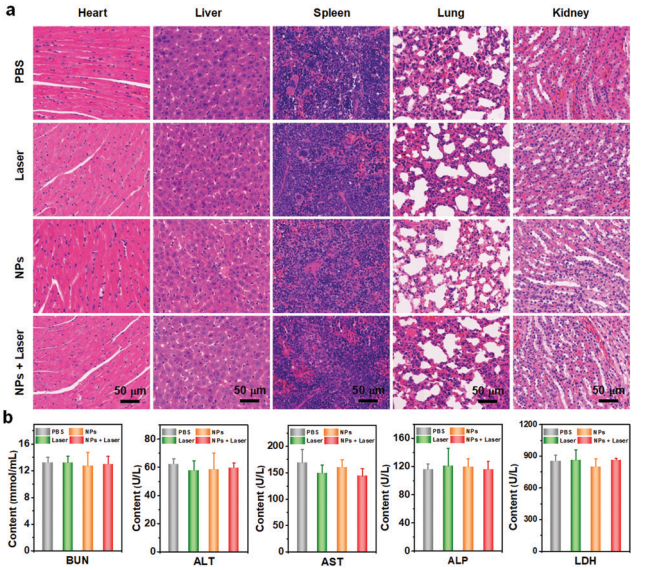

Fig. 5 (a) H&E staining of the main organs from the mice in the different groups. (b) Blood biochemistry analysis of the mice receiving different treatments.

other three kinds of treatment grew very quickly (Fig. 4c–e). This demonstrates the excellent tumor-killing ability of the ETTC NPs under laser irradiation, and reveals the superiority of combinational photodynamic and photothermal therapy. To further study the *in vivo* ROS generation of the ETTC NPs, tumor slice staining was conducted with the aforementioned ROS detection probe, DCFH-DA. This indicated that the only tumor slices from mice in the fourth group treated with NPs + laser showed strong green fluorescence from DCF, which was not observed in the other three groups (Fig. S14, ESI†), proving the *in vivo* PDT. H&E staining (Fig. 4f) showed no observable histopathological abnormalities in the tumors of mice treated with PBS, laser, and ETTC NPs, while destructive injuries were found in the tumor tissue of mice treated with NPs + laser.

Biosafety evaluation

The biosafety and biocompatibility of nanoagents are crucial parameters in biomedical research. Thus, we also conducted biosafety and biocompatibility evaluation for the ETTC NPs and the applied laser. The body weight of the mice were monitored after receiving different treatments every two days. During 14 days, the body weight of the mice in all the groups showed no significant difference, initially affirming the biocompatibility of the ETTC NPs and the applied laser (Fig. 4g). Furthermore, the main organs (heart, liver, spleen, lung, and kidney) of every group of mice were also collected at the 14th day after treatment for H&E staining. No observable abnormalities and injuries were noticed in any of organs in any group (Fig. 5a). Furthermore, we performed blood biochemical analysis for the treated mice. As indicated in Fig. 5b, there were no significant changes in the hematological indexes of the mice in the four groups. These results all illustrated the good biosafety and biocompatibility of the ETTC NPs and the applied laser.

Conclusions

We developed a coupled hardness with softness small molecule-based nanotheranostics system, which not only integrated photoacoustic and NIR-II fluorescence dual-modal imaging, but also could achieve photodynamic and photothermal synergistic cancer therapy upon 808 nm laser irradiation. This nanotherapeutic overcomes many problems that current multifunctional systems are confronted with, such as complex components, multi-light source employment, and low efficiency, which could be attributed to its simple construction and outstanding optical properties. The ETTC NPs showed outstanding light-harvesting ability, excellent photostability, and good biocompatibility. Most importantly, the ETTC NPs achieved a complete elimination of cancer cells *in vivo* under laser irradiation with the guidance of NIR-II and PA imaging. Therefore, this work provides a new idea for the design and development of versatile cancer nanomedicines by exploring single molecules.

Author contributions

Chun-Sing Lee, Shengliang Li, Jinfeng Zhang, and Xiaozhen Li designed the research; Xiaozhen Li synthesized the nanomaterials; Xiaozhen Li, Fang Fang and Bo Sun performed the biological research; Xiaozhen Li, Chao Yin, Yingpeng Wan and Pengfei Sun conducted all characterizations. Jihua Tan did calculations and analyzed results; Xiaozhen Li wrote the paper, and Chun-Sing Lee, Shengliang Li, Quli Fan, and Pengfei Wang made a revision of the paper.

Conflicts of interest

There are no conflicts to declare.

Acknowledgements

C.-S. L. would like to thank financial support by University Grants Committee/Research Grants Council of the Hong Kong Special Administrative Region, China (Project No. JLFS/P-101/18), ARG-CityU Applied Research Grant: Project no. 9667160, and ARG-CityU Applied Research Grant: Project no. 9667179. J. Z. would also like to acknowledge financial support by the Beijing Institute of Technology Research Fund Program for Young Scholars and the National Natural Science Foundation of China (Project No. 32001010). J. Z. would also like to thank Biological & Medical Engineering Core Facilities (Beijing Institute of Technology) for providing advanced equipment as well as The Young Elite Scientist Sponsorship Program of Beijing Association for Science and Technology (2021–2023).

Notes and references

1 E. Y. Lukianova-Hleb, Y.-S. Kim, I. Belatsarkouski, A. M. Gillenwater, B. E. O'Neill and D. O. Lapotko, *Nat. Nanotechnol.*, 2016, **11**, 525–532.
2 P. Wang, Y. Fan, L. Lu, L. Liu, L. Fan, M. Zhao, Y. Xie, C. Xu and F. Zhang, *Nat. Commun.*, 2018, **9**, 2898.
3 J. Qi, J. Li, R. Liu, Q. Li, H. Zhang, J. W. Y. Lam, R. T. K. Kwok, D. Liu, D. Ding and B. Z. Tang, *Chem*, 2019, **5**, 2657–2677.
4 S. H. Yun and S. J. J. Kwok, *Nat. Biomed. Eng.*, 2017, **1**, 0008.
5 K. K. Ng and G. Zheng, *Chem. Rev.*, 2015, **115**, 11012–11042.
6 J. Li and K. Pu, *Chem. Soc. Rev.*, 2019, **48**, 38–71.
7 D. Cui, J. Huang, X. Zhen, J. Li, Y. Jiang and K. Pu, *Angew. Chem., Int. Ed.*, 2019, **58**, 5920–5924.
8 M. Li, S. Long, Y. Kang, L. Guo, J. Wang, J. Fan, J. Du and X. Peng, *J. Am. Chem. Soc.*, 2018, **140**, 15820–15826.
9 W. Sun, X. Zhao, J. Fan, J. Du and X. Peng, *Small*, 2019, **15**, 1804927.
10 B. Guo, Z. Huang, Q. Shi, E. Middha, S. Xu, L. Li, M. Wu, J. Jiang, Q. Hu, Z. Fu and B. Liu, *Adv. Funct. Mater.*, 2020, **30**, 1907093.
11 B. Guo, Z. Sheng, D. Hu, C. Liu, H. Zheng and B. Liu, *Adv. Mater.*, 2018, **30**, 1802591.
12 W. Wu, D. Mao, S. Xu, M. Panahandeh-Fard, Y. Duan, F. Hu, D. Kong and B. Liu, *Adv. Funct. Mater.*, 2019, **29**, 1901791.
13 L. Jiang, H. Bai, L. Liu, F. Lv, X. Ren and S. Wang, *Angew. Chem., Int. Ed.*, 2019, **131**, 10770–10775.
14 H. Yuan, H. Chong, B. Wang, C. Zhu, L. Liu, Q. Yang, F. Lv and S. Wang, *J. Am. Chem. Soc.*, 2012, **134**, 13184–13187.
15 X. Li, L. Liu, S. Li, Y. Wan, J.-X. Chen, S. Tian, Z. Huang, Y.-F. Xiao, X. Cui, C. Xiang, Q. Tan, X.-H. Zhang, W. Guo, X.-J. Liang and C.-S. Lee, *ACS Nano*, 2019, **13**, 12901–12911.
16 S. Li, Q. Deng, X. Li, Y. Huang, X. Li, F. Liu, H. Wang, W. Qing, Z. Liu and C.-S. Lee, *Biomaterials*, 2019, **216**, 119252.
17 J. Ge, M. Lan, B. Zhou, W. Liu, L. Guo, H. Wang, Q. Jia, G. Niu, X. Huang, H. Zhou, X. Meng, P. Wang, C.-S. Lee, W. Zhang and X. Han, *Nat. Commun.*, 2014, **5**, 4596.
18 Y. Wan, G. Lu, J. Zhang, Z. Wang, X. Li, R. Chen, X. Cui, Z. Huang, Y. Xiao, J. Chelora, W. Zhang, Y. Liu, M. Li, H.-Y. Xie and C.-S. Lee, *Adv. Funct. Mater.*, 2019, **29**, 1903436.
19 C. Yin, X. Li, G. Wen, B. Yang, Y. Zhang, X. Chen, P. Zhao, S. Li, R. Li, L. Wang, C.-S. Lee and L. Bian, *Biomaterials*, 2020, **232**, 119684.
20 J. Zhang, J. Chen, J. Ren, W. Guo, X. Li, R. Chen, J. Chelora, X. Cui, Y. Wan, X.-J. Liang, Y. Hao and C.-S. Lee, *Biomaterials*, 2018, **181**, 92–102.
21 J. Zhang, C. Yang, R. Zhang, R. Chen, Z. Zhang, W. Zhang, S.-H. Peng, X. Chen, G. Liu, C.-S. Hsu and C.-S. Lee, *Adv. Funct. Mater.*, 2017, **27**, 1605094.
22 Y.-F. Xiao, J.-X. Chen, S. Li, W.-W. Tao, S. Tian, K. Wang, X. Cui, Z. Huang, X.-H. Zhang and C.-S. Lee, *Chem. Sci.*, 2020, **11**, 888–895.
23 S. Li, Q. Deng, Y. Zhang, X. Li, G. Wen, X. Cui, Y. Wan, Y. Huang, J. Chen, Z. Liu, L. Wang and C.-S. Lee, *Adv. Mater.*, 2020, 2001146, DOI: 10.1002/adma.202001146.
24 Y. Wan, G. Lu, W.-C. Wei, Y.-H. Huang, S. Li, J.-X. Chen, X. Cui, Y.-F. Xiao, X. Li, Y. Liu, X.-M. Meng, P. Wang, H.-Y. Xie, J. Zhang, K.-T. Wong and C.-S. Lee, *ACS Nano*, 2020, **14**(8), 9917–9928.
25 J. N. Liu, W. Bu and J. Shi, *Chem. Rev.*, 2017, **117**, 6160–6224.
26 M. Li, T. Xiong, J. Du, R. Tian, M. Xiao, L. Guo, S. Long, J. Fan, W. Sun, K. Shao, X. Song, J. W. Foley and X. Peng, *J. Am. Chem. Soc.*, 2019, **141**, 2695–2702.
27 Y. Liu, Y. Jiang, M. Zhang, Z. Tang, M. He and W. Bu, *Acc. Chem. Res.*, 2018, **51**, 2502–2511.
28 Q. Wang, Y. Dai, J. Xu, J. Cai, X. Niu, L. Zhang, R. Chen, Q. Shen, W. Huang and Q. Fan, *Adv. Funct. Mater.*, 2019, **29**, 1901480.
29 T. Sun, X. Chen, X. Wang, S. Liu, J. Liu and Z. Xie, *Mater. Chem. Front.*, 2019, **3**, 127–136.
30 X. Liu, H. Su, W. Shi, Y. Liu, Y. Sun and D. Ge, *Biomaterials*, 2018, **167**, 177–190.
31 Q. Wang, J. Xu, R. Geng, J. Cai, J. Li, C. Xie, W. Tang, Q. Shen, W. Huang and Q. Fan, *Biomaterials*, 2020, **231**, 119671.
32 Y. Wang, N. Gong, Y. Li, Q. Lu, X. Wang and J. Li, *J. Am. Chem. Soc.*, 2019, **142**, 1735–1739.
33 J. Sun, Y. Guo, R. Xing, T. Jiao, Q. Zou and X. Yan, *Colloids Surf., A*, 2017, **514**, 155–160.
34 Q. Sun, Q. You, X. Pang, X. Tan, J. Wang, L. Liu, F. Guo, F. Tan and N. Li, *Biomaterials*, 2017, **122**, 188–200.
35 S. Li, X. Wang, R. Hu, H. Chen, M. Li, J. Wang, Y. Wang, L. Liu, F. Lv, X.-J. Liang and S. Wang, *Chem. Mater.*, 2016, **28**, 8669–8675.
36 Y. Jiang, D. Cui, Y. Fang, X. Zhen, P. K. Upputuri, M. Pramanik, D. Ding and K. Pu, *Biomaterials*, 2017, **145**, 168–177.
37 T. Yang, L. Liu, Y. Deng, Z. Guo, G. Zhang, Z. Ge, H. Ke and H. Chen, *Adv. Mater.*, 2017, **29**, 1700487.
38 G. Hong, A. L. Antaris and H. Dai, *Nat. Biomed. Eng.*, 2017, **1**, 0010.

39 A. L. Antaris, H. Chen, K. Cheng, Y. Sun, G. Hong, C. Qu, S. Diao, Z. Deng, X. Hu, B. Zhang, X. Zhang, O. K. Yaghi, Z. R. Alamparambil, X. Hong, Z. Cheng and H. Dai, *Nat. Mater.*, 2016, **15**, 235–242.
40 Q. Miao and K. Pu, *Adv. Mater.*, 2018, **30**, 1801778.
41 J. Huang, C. Xie, X. Zhang, Y. Jiang, J. Li, Q. Fan and K. Pu, *Angew. Chem., Int. Ed.*, 2019, **58**, 15120–15127.
42 Y. Tang, Y. Li, X. Hu, H. Zhao, Y. Ji, L. Chen, W. Hu, W. Zhang, X. Li, X. Lu, W. Huang and Q. Fan, *Adv. Mater.*, 2018, **30**, 1801140.
43 Y. Tang, Y. Li, X. Lu, X. Hu, H. Zhao, W. Hu, F. Lu, Q. Fan and W. Huang, *Adv. Funct. Mater.*, 2019, **29**, 1807376.
44 H. Liu, G. Hong, Z. Luo, J. Chen, J. Chang, M. Gong, H. He, J. Yang, X. Yuan, L. Li, X. Mu, J. Wang, W. Mi, J. Luo, J. Xie and X.-D. Zhang, *Adv. Mater.*, 2019, **31**, 1901015.
45 R. Tian, Q. Zeng, S. Zhu, J. Lau, S. Chandra, R. Ertsey, K. S. Hettie, T. Teraphongphom, Z. Hu, G. Niu, D. O. Kiesewetter, H. Sun, X. Zhang, A. L. Antaris, B. R. Brooks and X. Chen, *Sci. Adv.*, 2019, **5**, eaaw0672.
46 S. Liu, C. Chen, Y. Li, H. Zhang, J. Liu, R. Wang, S. T. H. Wong, J. W. Y. Lam, D. Ding and B. Z. Tang, *Adv. Funct. Mater.*, 2019, **30**, 1908125.
47 Kenry, Y. Duan and B. Liu, *Adv. Mater.*, 2018, **30**, 1802394.
48 C. Sun, B. Li, M. Zhao, S. Wang, Z. Lei, L. Lu, H. Zhang, L. Feng, C. Dou, D. Yin, H. Xu, Y. Cheng and F. Zhang, *J. Am. Chem. Soc.*, 2019, **141**, 19221–19225.
49 Z. Lei, C. Sun, P. Pei, S. Wang, D. Li, X. Zhang and F. Zhang, *Angew. Chem., Int. Ed.*, 2019, **131**, 8250–8255.
50 Z. Sheng, B. Guo, D. Hu, S. Xu, W. Wu, W. H. Liew, K. Yao, J. Jiang, C. Liu, H. Zheng and B. Liu, *Adv. Mater.*, 2018, **30**, 1800766.
51 J. Zhang, X. Zhen, P. K. Upputuri, M. Pramanik, P. Chen and K. Pu, *Adv. Mater.*, 2017, **29**, 1604764.
52 C. Xie, X. Zhen, Y. Lyu and K. Pu, *Adv. Mater.*, 2017, **29**, 1703693.
53 Z. Yang, Y. Dai, C. Yin, Q. Fan, W. Zhang, J. Song, G. Yu, W. Tang, W. Fan, B. C. Yung, J. Li, X. Li, X. Li, Y. Tang, W. Huang, J. Song and X. Chen, *Adv. Mater.*, 2018, **30**, 1707509.
54 C. Yin, Y. Tang, X. Li, Z. Yang, J. Li, X. Li, W. Huang and Q. Fan, *Small*, 2018, **14**, 1703400.
55 C. Yin, G. Wen, C. Liu, B. Yang, S. Lin, J. Huang, P. Zhao, S. H. D. Wong, K. Zhang, X. Chen, G. Li, X. Jiang, J. Huang, K. Pu, L. Wang and L. Bian, *ACS Nano*, 2018, **12**, 12201–12211.
56 C. Yin, X. Zhen, Q. Fan, W. Huang and K. Pu, *ACS Nano*, 2017, **11**, 4174–4182.
57 C. Yin, X. Zhen, H. Zhao, Y. Tang, Y. Ji, Y. Lyu, Q. Fan, W. Huang and K. Pu, *ACS Appl. Mater. Interfaces*, 2017, **9**, 12332–12339.
58 Y. Wang, T. Yang, H. Ke, A. Zhu, Y. Wang, J. Wang, J. Shen, G. Liu, C. Chen, Y. Zhao and H. Chen, *Adv. Mater.*, 2015, **27**, 3874–3882.
59 Y. Cai, P. Liang, Q. Tang, X. Yang, W. Si, W. Huang, Q. Zhang and X. Dong, *ACS Nano*, 2017, **11**, 1054–1063.
60 J. Mou, T. Lin, F. Huang, H. Chen and J. Shi, *Biomaterials*, 2016, **84**, 13–24.
61 C. Chen, H. Ou, R. Liu and D. Ding, *Adv. Mater.*, 2020, **32**, 1806331.
62 D. Zhang, M. Wu, Y. Zeng, N. Liao, Z. Cai, G. Liu, X. Liu and J. Liu, *J. Mater. Chem. B*, 2016, **4**, 589–599.
63 Q. Jia, J. Ge, W. Liu, S. Liu, G. Niu, L. Guo, H. Zhang and P. Wang, *Nanoscale*, 2016, **8**, 13067–13077.
64 S. Dai, T. Li, W. Wang, Y. Xiao, T.-K. Lau, Z. Li, K. Liu, X. Lu and X. Zhan, *Adv. Mater.*, 2018, **30**, 1706571.
65 S. Dai, T. Li, W. Wang, Y. Xiao, T.-K. Lau, Z. Li, K. Liu, X. Lu and X. Zhan, *Adv. Mater.*, 2018, **30**, 1706571.
66 V.-N. Nguyen, Y. Yim, S. Kim, B. Ryu, K. M. K. Swamy, G. Kim, N. Kwon, C.-Y. Kim, S. Park and J. Yoon, *Angew. Chem., Int. Ed.*, 2020, **59**, 8957–8962.
67 S. Xu, Y. Yuan, X. Cai, C.-J. Zhang, F. Hu, J. Liang, G. Zhang, D. Zhang and B. Liu, *Chem. Sci.*, 2015, **6**, 5824–5830.
68 J. Zhang, W. Chen, R. Chen, X.-K. Liu, Y. Xiong, S. V. Kershaw, A. L. Rogach, C. Adachi, X. Zhang and C.-S. Lee, *Chem. Commun.*, 2016, **52**, 11744–11747.
69 Z. Zhao, C. Chen, W. Wu, F. Wang, L. Du, X. Zhang, Y. Xiong, X. He, Y. Cai, R. T. K. Kwok, J. W. Y. Lam, X. Gao, P. Sun, D. L. Phillips, D. Ding and B. Z. Tang, *Nat. Commun.*, 2019, **10**, 768.
70 Z. Zhang, W. Xu, M. Kang, H. Wen, H. Guo, P. Zhang, L. Xi, K. Li, L. Wang, D. Wang and B. Z. Tang, *Adv. Mater.*, 2020, **32**, 2003210.
71 K. Pu, J. Mei, J. V. Jokerst, G. Hong, A. L. Antaris, N. Chattopadhyay, A. J. Shuhendler, T. Kurosawa, Y. Zhou, S. S. Gambhir, Z. Bao and J. Rao, *Adv. Mater.*, 2015, **27**, 5184–5190.
72 Z. Sun, H. Xie, S. Tang, X.-F. Yu, Z. Guo, J. Shao, H. Zhang, H. Huang, H. Wang and P. K. Chu, *Angew. Chem., Int. Ed.*, 2015, **54**, 11526–11530.
73 J. T. Robinson, S. M. Tabakman, Y. Liang, H. Wang, H. Sanchez Casalongue, D. Vinh and H. Dai, *J. Am. Chem. Soc.*, 2011, **133**, 6825–6831.
74 Z. Tao, G. Hong, C. Shinji, C. Chen, S. Diao, A. L. Antaris, B. Zhang, Y. Zou and H. Dai, *Angew. Chem., Int. Ed.*, 2013, **52**, 13002–13006.